

Cite this: *J. Mater. Chem. A*, 2023, **11**, 7077

Terpyridine-zinc(II) coordination nanosheets as modulators of perovskite crystallization to enhance solar cell efficiency†

Ying-Chiao Wang,^a Chun-Hao Chiang,^b Chun-Jen Su,^c Je-Wei Chang,^c Chi-Ying Lin,^b Chia-Chun Wei,^d Shao-Ku Huang,^b Hiroaki Maeda,^e Wen-Bin Jian,^d U-Ser Jeng,^{cf} Kazuhito Tsukagoshi,^g Chun-Wei Chen^{bg} and Hiroshi Nishihara^{*e}

The high efficiency of precursor-to-perovskite conversion is one of the core factors in boosting the performance of perovskite solar cells (PSCs). Herein, we report a liquid/liquid interfacial synthesis of terpyridine-zinc(II) (ZnTPY) coordination nanosheets (CONASHs), which can enhance PbI₂-based perovskite crystallization and thus the efficiency of PSCs. Ultrasonically fragmented ZnTPY CONASHs, rich in uncoordinated terpyridine moieties, caused multidentate chelation with PbI₂, resulting in a well-dispersed ZnTPY:PbI₂ complex. This metal-organic complex could act as a heterogeneous nucleation seed and facilitate the formation of a PbI₂-to-[PbI_{6-x}]⁴⁻ coordinated octahedral framework in a precursor solution of perovskite, thereby reducing the crystallization barrier of tetragonal CH₃NH₃PbI₃ perovskites and achieving a complete precursor-to-perovskite conversion. Consequently, ZnTPY-capped perovskite crystals had a long photoluminescence (PL) lifetime, which is attributed to the more passivated trap states associated with ZnTPY. The corresponding PSCs exhibited an optimal power conversion efficiency of 19.8% compared with 17.9% of the controlled device. The results prove that the performance of PSC families can be improved by dispersing PbI₂ in a solution with CONASHs for enhancing the PbI₂-to-perovskite conversion.

Received 29th January 2023
Accepted 1st March 2023

DOI: 10.1039/d3ta00505d

rsc.li/materials-a

Introduction

Over the past 10 years of research and development, organo-metallic halide perovskite solar cells (PSCs) have emerged as the fastest-growing photovoltaic system, with a certified power conversion efficiency (PCE) of over 25%.¹ One of the key factors in the fabrication of high-efficiency PSCs is the preparation of

highly crystalline perovskites with a more uniform film morphology and fewer defects in nonradiative recombination.^{2–4} In particular, the quality of perovskites highly depends on the crystallization process, which in turn is determined by compound factors that reduce the activation energy of crystallization in general. Accordingly, several crystal engineering strategies have been adopted to reduce the activation energy of perovskite nucleation and growth by implanting tailored electron transport layers (ETLs) containing heterogeneous nuclei.^{5,6} Nevertheless, embedding crystallization nuclei at the interface between the ETL and the perovskite film is limited to this two-dimensional (2D) interface. To increase the number of perovskite nucleation seeds, we recently reported an intermixing-seeded growth technique using iodide ion-capped PbS nanoparticles as seed-like nucleation centers to reduce the energy barrier of precursor-to-perovskite crystallization.^{7,8} By accelerating the formation of inorganic [PbI_{6-x}]⁴⁻ nuclei and reducing the activation energy of precursor-to-perovskite conversion, from 145 ± 38 to 47 ± 5 kJ mol⁻¹, the crystallinity of perovskite crystals and the solar cell performance of PbS-treated PSCs were both significantly improved. Notably, PbS nanoparticles need a ligand exchange treatment to improve their solubility in perovskite precursors. However, the oleic acid-based long-chain ligands around the initial PbS

^aInternational Center for Young Scientists (ICYS) and WPI International Center for Materials Nanoarchitectonics (WPI-MANA), National Institute for Materials Science (NIMS), Tsukuba, Ibaraki 305-0044, Japan. E-mail: TSUKAGOSHI.Kazuhito@nims.go.jp

^bDepartment of Materials Science and Engineering, National Taiwan University, Taipei 10617, Taiwan. E-mail: chunwei@ntu.edu.tw

^cNational Synchrotron Radiation Research Center, Hsinchu Science Park, Hsinchu 30076, Taiwan. E-mail: usjeng@nsrrc.org.tw

^dDepartment of Electrophysics, National Yang Ming Chiao Tung University, Hsinchu 30010, Taiwan

^eResearch Institute for Science and Technology, Tokyo University of Science, Chiba 278-8510, Japan. E-mail: nishihara@rs.tus.ac.jp

^fDepartment of Chemical Engineering, National Tsing Hua University, Hsinchu 30013, Taiwan

^gCenter of Atomic Initiative for New Materials (AI-MAT), National Taiwan University, Taipei 10617, Taiwan

† Electronic supplementary information (ESI) available: Experimental section and additional figures. See DOI: <https://doi.org/10.1039/d3ta00505d>

nanoparticles could not be completely replaced by iodide ions, and the residual part became a source of defect sites in the PSCs; hence, new heterogeneous nucleation materials with no residual ligand effect are needed for perovskite crystallization.

The recently discovered π -conjugated coordination nanosheets (CONASHs), consisting of organic ligands and metal parts in a 2D polymeric network, have demonstrated various surprising chemical, optical, and electronic properties due to their tunable molecular components.^{9–12} Interestingly, CONASHs are rich in conducting π -ligands and can possibly be mixed with perovskite precursor solutions as crystallization seeds with no need for the alkyl ligand substitution process previously mentioned; moreover, they are expected to facilitate charge transportation. Recently, benefiting from the conductivity and material variability of CONASHs, we synthesized a UV-sensitized bis(dithiolene)iron(II) complex motif by combining benzenehexathiol (BHT) ligands and iron(II) ions to fabricate a self-powered photodetector, which exhibited a spectral responsivity of 6.57 mA W^{-1} under 365 nm light radiation.¹³ Additionally, once the size of the ligands increases, more CONASHs with different structures and photofunctions can be designed because of the customized steric hindrance. For example, after replacing the small-sized BHT with a large-molecule three-way terpyridine (TPY), the extended molecular space between TPYs allowed accommodating larger ZnSO_4 molecules.¹⁴ Compared with Zn(II) ions, the CONASH comprising ZnSO_4 showed a red-shifted luminescence of 480 to 552 nm. In this work, a CONASH consisting of ZnSO_4 and TPY ligands (ZnTPY) was synthesized and fragmented into PbI_2 -based PSCs for heterogeneous crystallization nuclei. We observed that the TPY- ZnSO_4 coordination interaction was

weak because of the steric hindrance imposed by the TPY molecules. Therefore, upon ultrasonic vibration, chemical bonds between TPY and ZnSO_4 at the ZnTPY edges would break and expose the TPY-only terminal group (that is, TPY uncoordinated sites). Through multidentate chelation of TPY-only edges to PbI_2 after introducing these ZnTPY fragments into the perovskite precursors, ZnTPY:PbI_2 heterogeneous nuclei with a lower energy barrier were preferentially nurtured. Consequently, the precursor-to-perovskite conversion and crystallinity could be significantly improved. Accordingly, the ZnTPY-modified PSC yielded an enhanced PCE of 19.8%, compared with 17.9% for the reference device. This work provides a new and general concept of using 2D CONASHs as an additive in the development of organic photovoltaic devices.

Results and discussion

Synthesis of fractured ZnTPY CONASHs

Fig. 1a shows the chemical formula for growing ZnTPY CONASHs. The threefold symmetric ligand structure is given as TPY, 1,3,5-tris[4-(4'-2,2':6',2''-terpyridyl)phenyl]-benzene. Furthermore, $\text{Zn(NH}_4)_2(\text{SO}_4)_2$ was used as the zinc source, and the ZnTPY product was characterized as the $\text{TPY-Zn(II)-(SO}_4)_2\text{-Zn(II)-TPY}$ complex motif, as shown in Fig. 1a. The remaining ammonium sulfate $[(\text{NH}_4)_2\text{SO}_4]$ can be removed from the ZnTPY CONASHs by washing. Before the synthesis reaction started, the TPY molecule was dispersed in dichloromethane (CH_2Cl_2), as shown in Fig. 1b. Subsequently, the aqueous solution containing the dissolved Zn source and NaBr charge compensator was carefully injected drop by drop on top of the TPY solution. Through bottom-up liquid/liquid interfacial coordination

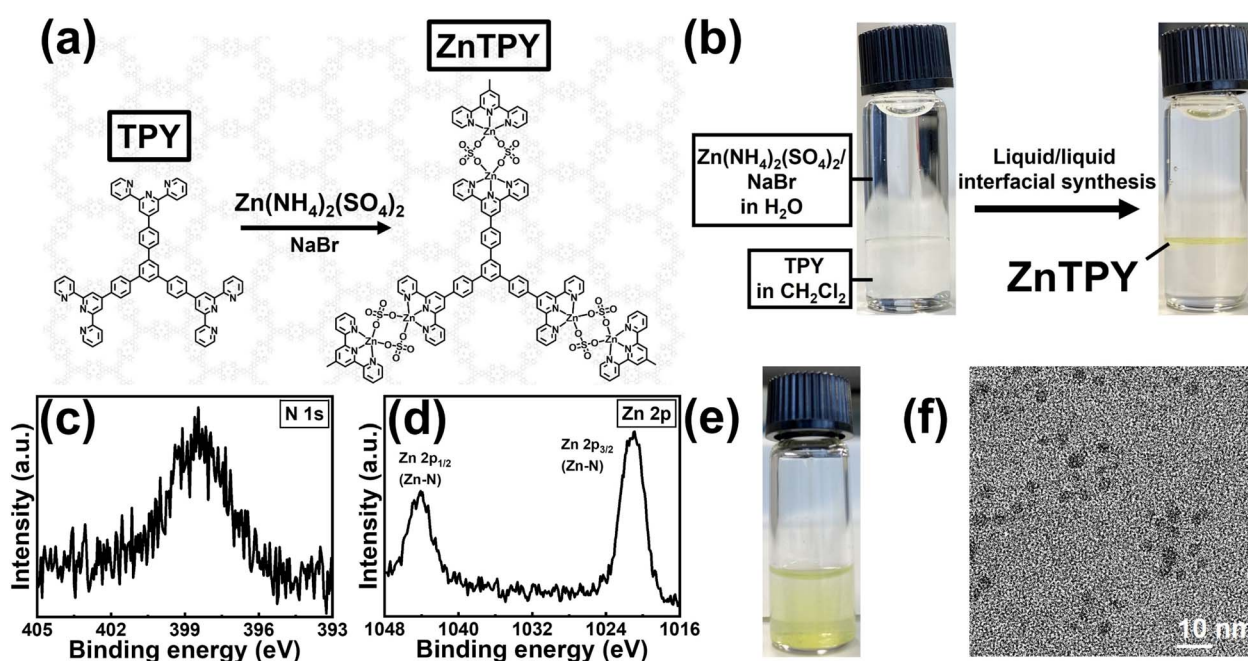


Fig. 1 Fragmentation and characterization of the ZnTPY CONASHs. (a) Schematic illustration of the polymerization of the ZnTPY CONASHs. (b) Photographs of the synthesis at the liquid/liquid interface. High-resolution XPS of (c) N 1s and (d) Zn 2p core levels of the as-synthesized ZnTPY CONASHs. (e) A representative photograph of shattered ZnTPY nanosheets dispersed in DMF solvent and (f) the corresponding TEM image.

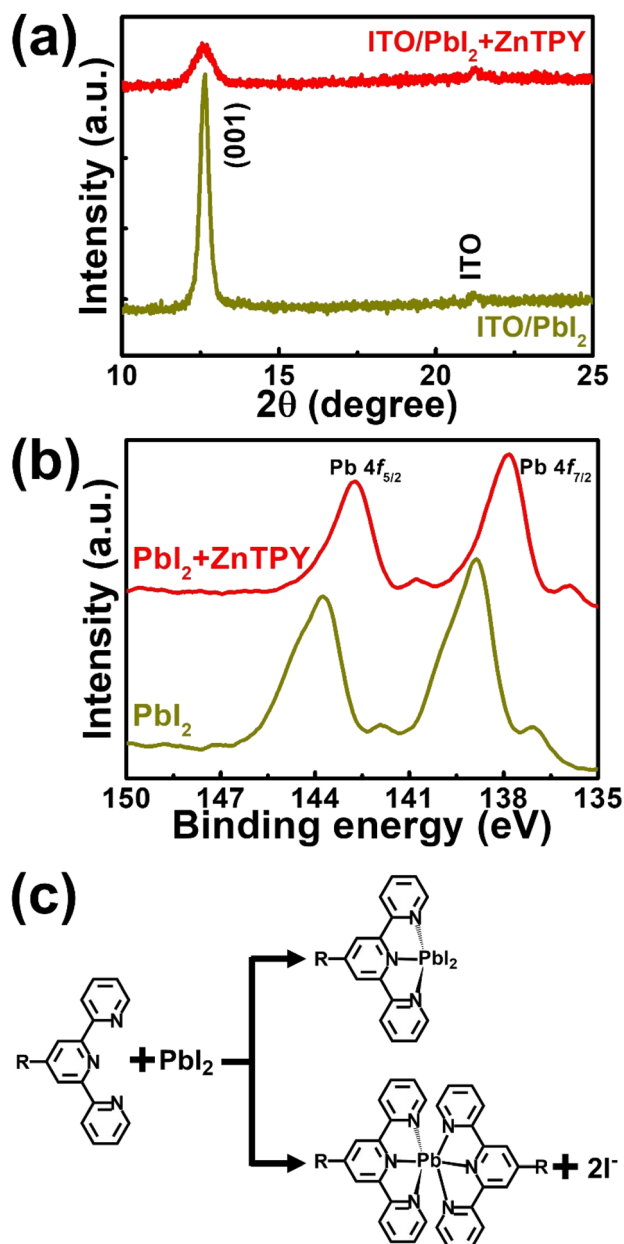


Fig. 2 Chelation of PbI₂ with ZnTPY nanosheets. (a) XRD patterns of ITO/PbI₂ and ITO/PbI₂/ZnTPY films. (b) High-resolution XPS of the Pb 4f core level of the bare PbI₂ and PbI₂/ZnTPY samples. (c) Two possible routes of the formation of ZnTPY:PbI₂ adducts.

synthesis, electrostatic attraction occurred between TPY and ZnSO₄, followed by spontaneous assembly of pale yellow ZnTPY CONASHs. After removal of the biphasic solvents and transfer to the target substrate, ZnTPY showed wide continuity with a thickness of approximately 12 nm (Fig. S1, ESI[†]) under a transmission electron microscope (TEM) and atomic force microscope (AFM). Moreover, X-ray photoelectron spectroscopy (XPS) was performed to characterize the bonding properties of ZnTPY CONASHs. As presented in Fig. 1c, the N 1s spectrum at 398.5 eV can be attributed to the nitrogen signal of pyridine,^{15,16} meaning that the ZnTPY was filled with pyridine-based TPY groups. As revealed from Fig. 1d, the doublet peaks of high-

resolution Zn 2p spectra distributed at 1021.1 and 1044.2 eV prove the presence of Zn–N bonds,¹⁷ indicating that TPY ligands grow into ZnTPY films by a coordination reaction with the Zn(II) part of ZnSO₄. Subsequently, ZnTPY CONASHs were fragmented and added to the perovskite precursor solution of PbI₂, as the fragmented ZnTPY can expose more uncoordinated TPY groups to chelate with PbI₂ in the solution. The synthesized CONASHs were dispersed in dimethylformamide (DMF) and subjected to ultrasonic treatment for 1 h for fragmented ZnTPY less than 10 nm in size, as shown in Fig. 1e and f. Next, these well-dispersed ZnTPY nano-nuclei in DMF were added to the same solvent of the perovskite precursor solution.

Heterogeneous nuclei

CH₃NH₃PbI₃ perovskite was produced by the reaction of inorganic PbI₂ with organic CH₃NH₃I, and the crystallization process could be modulated by the activation energy of nucleation.⁷ In this process, the formation of [PbI₆]⁴⁻ octahedra had a high energy barrier, especially when PbI₂ preorders into a hexagonal phase.^{18,19} In the case without ZnTPY, dispersed Pb²⁺ interacted with I⁻ ions in a solution of dissociated precursors (*e.g.*, Pb²⁺ + 2I⁻ or CH₃NH₃⁺ + I⁻) and formed [PbI₆]⁴⁻, whereas PbI₂ formed an ordered phase. Introducing ZnTPY CONASHs into a solution of PbI₂ effectively dispersed PbI₂ from hexagonal packing, thereby reducing the perovskite crystallization energy barrier.

In our case, the solutions of PbI₂ or ZnTPY:PbI₂ adducts were spin-coated onto indium tin oxide (ITO)/glass substrates and then annealed at 100 °C for 10 min in a N₂-purged glovebox to remove the DMF solvent. Hence, the X-ray diffraction (XRD) pattern in Fig. 2a shows a typical hexagonal 2H polytype PbI₂ signal at a scattering angle $2\theta = 12.6^\circ$, corresponding to the (001) plane.²⁰ In contrast, the intensity of the diffraction peak in the (001) reflection of the ITO/ZnTPY:PbI₂ sample was greatly suppressed. This is attributed to the facile insertion of ZnTPY into PbI₂ aggregates through multidentate chelation, leading to dispersion of [(PbI_{6-x})^{4-x-}–ZnTPY]. XPS was used to confirm the chemical interactions between ZnTPY and PbI₂. As illustrated in Fig. 2b, the Pb core level 4f_{7/2} and 4f_{5/2} peaks of the ZnTPY:PbI₂ film were shifted toward lower binding energies compared with the pristine PbI₂ film, indicating that the increase in valence electrons around ZnTPY-covered Pb atoms led to an enhanced electrostatic shielding effect and therefore lowered the binding energy of electrons.²¹ This phenomenon can be interpreted as a chelation effect of the uncoordinated TPY groups of ZnTPY CONASHs (acting as the Lewis base to provide additional lone-pair electrons for Pb atoms) on the formation of ZnTPY:PbI₂.

On the basis of the chemical structure of ZnTPY and the above reaction analysis, two possible routes for the formation of the ZnTPY:PbI₂ complex are proposed, as schematically demonstrated in Fig. 2c. Namely, the uncoordinated TPY sites of the broken ZnTPY edges created a TPY–PbI₂ tridentate (that is, the reaction of lead(II) with a single TPY molecule)²² or TPY–Pb(II)–TPY hexadentate (that is, the reaction of lead(II) with a pair of TPY molecules) chelation with lead(II) instead of the iodide ion originally located at the corner of the [PbI₆]⁴⁻ octahedron.

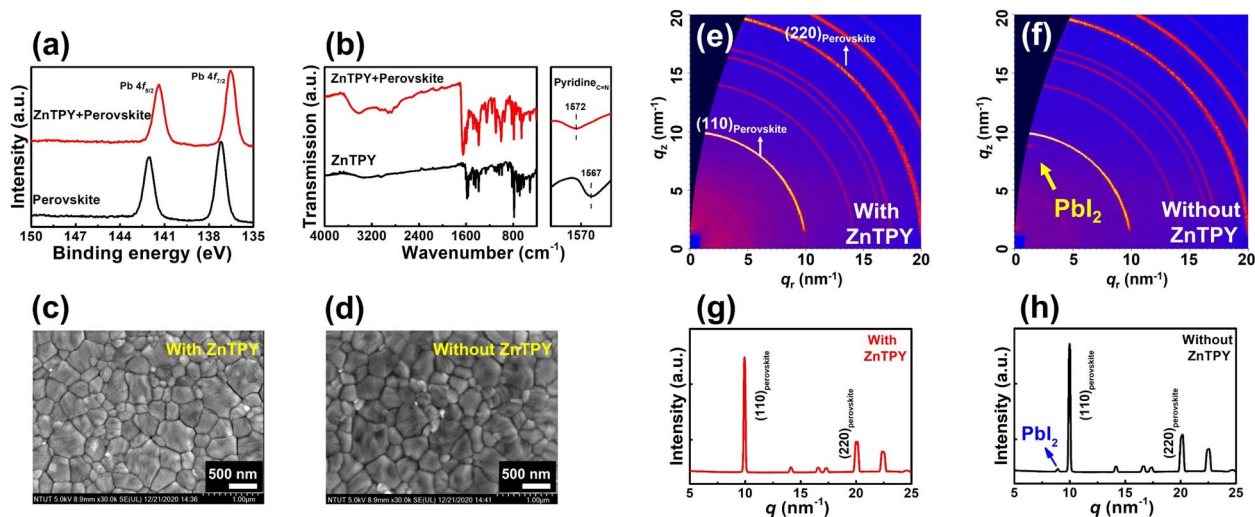


Fig. 3 Properties of perovskite crystals with ZnTPY fragments. (a) High-resolution XPS of the Pb 4f core level of the $\text{CH}_3\text{NH}_3\text{PbI}_3$ perovskites with and without ZnTPY. (b) FTIR spectra of $\text{CH}_3\text{NH}_3\text{PbI}_3$ perovskite and the ZnTPY-perovskite hybrid. (c) and (d) SEM morphologies of $\text{CH}_3\text{NH}_3\text{PbI}_3$ films with and without ZnTPY, respectively. (e) and (f) 2D GIXS spectra of perovskite films with and without ZnTPY fragment addition; (g) and (h) the corresponding integrated 1D GIXS patterns.

Presumably, the chelation can disperse PbI_2 from its layering packing, thereby reducing the crystallization barrier of perovskite. The ZnTPY: PbI_2 chelated octahedral structure could further serve as a heterogeneous nucleus in perovskite structure formation.^{23,24}

Characterization of ZnTPY-perovskite films

The next step is to examine the possibility of improving the crystallinity of $\text{CH}_3\text{NH}_3\text{PbI}_3$ perovskite crystals by introducing ZnTPY: PbI_2 heterogeneous nuclei. Previous results show that the reaction site with PbI_2 is mainly located at the uncoordinated TPY ligand of the small-sized ZnTPY terminal group. Compared with the TPY ligand-only system, the uncoordinated pyridine content of ZnTPY is much reduced because most of the TPY molecules coordinate with ZnSO_4 to form 2D CONASHs. Consequently, the addition of the pure TPY ligand will gelatinize the perovskite precursor solution (Fig. S2, ESI†), blocking subsequent solution processes. Therefore, ZnTPY fractions (1 wt%) were added to the perovskite precursor, and the $\text{CH}_3\text{NH}_3\text{PbI}_3$ perovskite film was fabricated by spin-coating and annealing. XPS measurements were performed on pristine perovskite and ZnTPY-treated perovskite films to understand the interaction between ZnTPY and Pb(II) ions, which is consistent with the previous observation on PbI_2 and ZnTPY: PbI_2 . Compared with the pristine perovskites, the Pb 4f signals of the ZnTPY-treated perovskite film shifted to a lower core-level bonding energy, indicating that the ZnTPY additive increases the valence electrons around the lead(II) to carry out the chelation reaction, as depicted in Fig. 3a. The chemical structures of ZnTPY: PbI_2 complexes were further analyzed by Fourier transform infrared (FTIR) spectroscopy, revealing a signature of the pristine ZnTPY-CONASH peak at 1567 cm^{-1} which corresponds to the stretching vibration of the $\text{C}=\text{N}$ bond from pyridine rings (Fig. 3b).²⁵ This $\text{C}=\text{N}$ functional group is the

terminal site used by TPY to chelate with lead(II). Once perovskite crystals were added, the $\text{C}=\text{N}$ peak shifted to 1572 cm^{-1} . The chemically induced shift toward the larger wavenumber suggested a coordination reaction between pyridine molecules and metal ions,²⁶ implying the formation of ZnTPY: PbI_2 adducts.

After investigating the PbI_2 dispersion effect of the CONASHs on ZnTPY: PbI_2 complexes in perovskite crystals, we examined the effect of ZnTPY: PbI_2 complex addition on the growth of $\text{CH}_3\text{NH}_3\text{PbI}_3$ perovskite films. All perovskite films were deposited on ITO glass and then spin-coated at 5000 rpm for 30 s in a N_2 -filled atmosphere. The chlorobenzene (CB) antisolvent approach was performed 8 s after the start of spin-coating. Finally, the films were annealed at 100°C for 10 min. Fig. 3c and d present the top-view scanning electron microscope (SEM) images of perovskite crystals prepared with and without ZnTPY CONASHs, respectively. These two SEM images exhibit similar grain sizes. Nevertheless, with the addition of ZnTPY in Fig. 3c, the sharper lattice fringes and more homogeneous contrast of the perovskites indicate smoother surfaces for a more uniform crystallization nature,²⁷ compared with those without ZnTPY in Fig. 3d.

To gain more insight into the association between the ZnTPY additive and the crystallinity of perovskites, grazing-incidence X-ray scattering (GIXS) spectra were recorded.^{7,8} The preparation procedure of the perovskite films was the same as the SEM samples except that the ITO substrate was replaced by a silicon wafer with low GIXS background scattering. Fig. 3e and f show the 2D GIXS profiles of the perovskite films, respectively, with and without 1 wt% of fractured ZnTPY CONASHs. The observed scattering reflections of perovskite crystals could be indexed to the typical orthorhombic structure of $\text{CH}_3\text{NH}_3\text{PbI}_3$ perovskite;²⁸ both films exhibited similar polycrystalline structures of the perovskite crystals. In addition, these perovskite films were both subjected to CB antisolvent drop-washing during the spin-

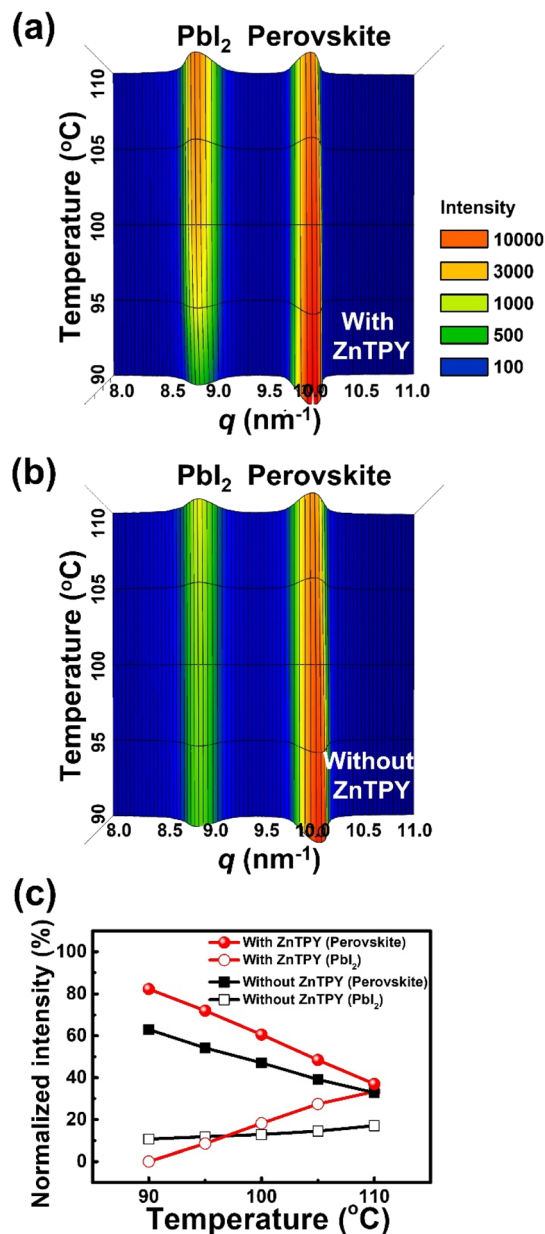


Fig. 4 Temperature-dependent GIXS analysis of $\text{CH}_3\text{NH}_3\text{PbI}_3$ films during thermal annealing. The temperature-dependent GIXS profiles of (a) $\text{CH}_3\text{NH}_3\text{PbI}_3\text{:ZnTPY}$ and (b) pristine $\text{CH}_3\text{NH}_3\text{PbI}_3$ films, displaying the growth of the PbI_2 peak center at $q = 8.9 \text{ nm}^{-1}$ and the decay of the perovskite (110) peak at $q = 10 \text{ nm}^{-1}$. (c) Evolution of the normalized perovskite (110) peak intensity and the relative PbI_2 peak intensity.

coating process to accelerate the nucleation of the perovskite precursors, which induced supersaturation-driven growth of perovskite films with preferred orientation along the out-of-plane directions.²⁹ Hence, the (110) and (220) reflections in the 2D GIXS patterns of both the perovskite crystallization with ZnTPY and the pristine perovskite film enhanced more along the out-of-plane direction (q_z) than along the in-plane direction (q_r). However, the perovskite-only sample showed a residual PbI_2 ordering peak at $q_z = 8.9 \text{ nm}^{-1}$ in the pattern (Fig. 3f) and

corresponding profile (Fig. 3h), which is the residual PbI_2 that failed in the conversion into perovskite crystals. By contrast, no PbI_2 hexagonal phase was observed with ZnTPY addition (Fig. 3e and g), which confirms that ZnTPY CONASHs improve the efficiency of the precursor-to-perovskite conversion.

Thermal stability of ZnTPY-perovskite

In addition to crystallinity, thermal stability also improved because of the ZnTPY seeds on the perovskite crystals, as illustrated by temperature-resolved GIXS. Perovskite thin films deposited onto silicon wafers with and without ZnTPY were sealed in a humidity-controlled chamber and measured during successive 10 min thermal annealing at 90 °C to 110 °C (Fig. 4). At 90 °C annealing, the perovskite (110) peak of the film processed with CONASHs can maintain *ca.* 90% of the original peak intensity measured at room temperature, and no PbI_2 signature peak was observed at $q = 8.9 \text{ nm}^{-1}$. In contrast, the (110) peak of the film without CONASHs decayed to 60%, and the PbI_2 signature of enhanced intensity was observed. Overall, between 90 °C and 110 °C, the (110) peak of the ZnTPY-processed film maintained better thermal stability. However, between 95 °C and 110 °C, the PbI_2 signature peak of the film with ZnTPY emerged and grew quickly compared with that of the film processed without ZnTPY, revealing a higher quantity of PbI_2 in the perovskite formation. Namely, a higher precursor-to-perovskite conversion ratio could be achieved by introducing ZnTPY-based heterogeneous nuclei. This phenomenon is consistent with the aforementioned conclusion that ZnTPY CONASHs can coordinate to lead(II) and thus PbI_2 precursors for a higher efficiency of perovskite conversion. Meanwhile, ZnTPY- PbI_2 chelating formation also led to higher thermal stability of the ZnTPY-embedded perovskite crystals.

Photoelectric properties

To reveal the effect of improved crystallinity of perovskite crystals on optoelectronic devices, we fabricated ZnTPY-modified PSCs, where the corresponding device configuration was ITO glass/ SnO_2 /CPTA/perovskite/Spiro-OMeTAD/Au. Among them, SnO_2 and CPTA form an electron transport bilayer, and Spiro-OMeTAD is the hole transport layer. The cross-sectional SEM images of PSCs with and without ZnTPY show a similar layered structure (Fig. S3, ESI†). The thickness of perovskite layers inside these two PSCs is very similar, around 530 nm. However, the perovskite layer after the addition of ZnTPY has a smoother morphology and a more uniform layer structure than the pristine perovskite film. This result is consistent with top viewed-SEM observations in Fig. 3c and d. Fig. 5a illustrates the current density-voltage (J - V) measurements of PSCs with and without ZnTPY nuclei under simulated one-sun illumination (100 mW cm^{-2}). The optimal J - V parameters are listed in Table 1. Since charge carrier transporters were combined with the same energy band structure, the PSC devices showed a similar open circuit voltage (V_{OC}) of approximately 1.12 V. The best PSC incorporating 1% fractured ZnTPY CONASHs as seeds inside the perovskite layer yielded a PCE of 19.8% with a short-circuit current density (J_{SC}) of 22.32 mA cm^{-2} and a fill factor (FF) of

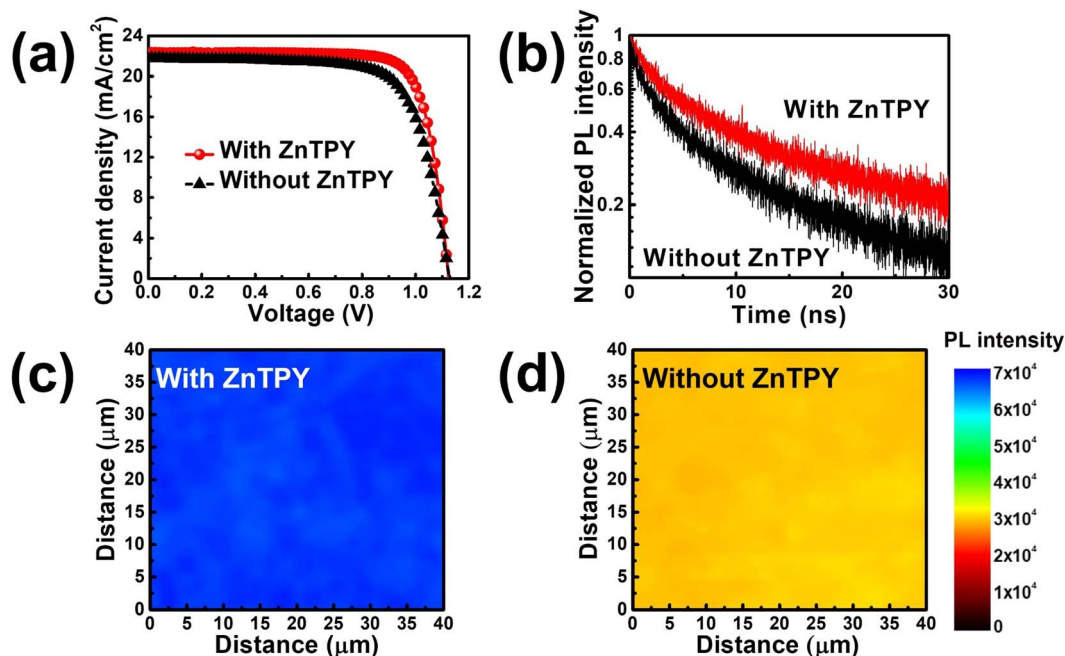


Fig. 5 Photovoltaic properties. (a) J - V profiles of the best PSC devices with and without ZnTPY fragments under AM 1.5G illumination (100 mW cm^{-2}). (b) TRPL decay plots of $\text{CH}_3\text{NH}_3\text{PbI}_3\text{:ZnTPY}$ and pristine $\text{CH}_3\text{NH}_3\text{PbI}_3$ samples. PL maps recorded for the as-deposited films of (c) $\text{CH}_3\text{NH}_3\text{PbI}_3\text{:ZnTPY}$ and (d) $\text{CH}_3\text{NH}_3\text{PbI}_3$ perovskite only.

79.1%. Nevertheless, the device performance decreased significantly when no additive was added during the synthesis of the perovskite film, exhibiting a PCE of 17.9%, a J_{SC} of 21.75 mA cm^{-2} , and a FF of 73.1%. The average data are summarized in Table 1, which indicates that the reproducibility of the PSC devices is sufficiently high. The relative enhancement of the J_{SC} value in the ZnTPY-seeded PSC may contribute to a higher precursor-to-perovskite conversion ratio (Fig. 4a), and the increment of perovskite photosensitizers can be used to absorb more sunlight to generate extra free photogenerated carriers. According to the literature, reducing the nonradiative recombination of excess PbI_2 helps to increase the FF value.^{30,31} This is consistent with the previously mentioned absence of PbI_2 ordered domains from the ZnTPY-treated perovskite film, as revealed in the previous GIXS result (Fig. 3e).

Furthermore, we examined the lifetimes of photocarriers to explore the relationship between the modified crystallinity and increased photovoltaic efficiency. The time-resolved photoluminescence (TRPL) decay curves in Fig. 5b indicate the photocarrier dynamics. These TRPL results showed the two-step-exponential-decay property of recombination,³² where each profile could be deconvoluted into two stages of two different characteristic lifetimes. The TRPL lifetimes and corresponding

Table 2 TRPL lifetimes of quartz/perovskite films with and without ZnTPY CONASHs

| Devices | τ_1 (ns) | Fraction 1 (%) | τ_2 (ns) | Fraction 2 (%) | τ_{Average} (ns) |
|---------------|---------------|----------------|---------------|----------------|------------------------------|
| With ZnTPY | 10.02 | 67.30 | 57.03 | 32.70 | 25.39 |
| Without ZnTPY | 4.962 | 71.76 | 37.20 | 28.24 | 14.07 |

amplitudes are summarized in Table 2. In the table, τ_1 and τ_2 are, respectively, the fast and slow photocarrier decay lifetimes after excitation for a long time. Moreover, the amplitude-weighted averaging (τ_{Average}) of these two TRPL parameters gives an average lifetime. The pristine perovskite sample showed a τ_{Average} of 14.07 ns, whereas the τ_{Average} of the ZnTPY-seeded perovskite film increased dramatically by nearly twofold to 25.39 ns. The $\text{CH}_3\text{NH}_3\text{PbI}_3$ perovskite layers incorporating the ZnTPY heterogeneous nucleation sites exhibited a longer PL average lifetime, indicating that more photocarriers were generated due to the formation of better crystal quality resulting in fewer defect states. The TRPL decay results showed a trend consistent with the PSC device performances. To confirm the uniformity of the ZnTPY seeding effect inside perovskite films,

Table 1 Photovoltaic parameters of PSCs with and without ZnTPY CONASHs measured at 100 mW cm^{-2} under simulated AM 1.5G illumination. Average and standard deviation data collected in brackets were statistically obtained from 6 different PSCs

| Devices | V_{OC} (V) | J_{SC} (mA cm^{-2}) | FF (%) | PCE (%) |
|---------------|-----------------------------|---|---------------------------|---------------------------|
| With ZnTPY | 1.123 (1.123 ± 0.011) | 22.32 (22.26 ± 0.26) | 79.1 (78.22 ± 0.75) | 19.8 (19.55 ± 0.21) |
| Without ZnTPY | 1.126 (1.109 ± 0.010) | 21.75 (21.24 ± 0.58) | 73.1 (72.95 ± 0.87) | 17.9 (17.18 ± 0.60) |

we plotted the 2D mapping of PL intensities. Fig. 5c and d depict the 2D PL mapping of perovskite thin films with and without ZnTPY nuclei insertion, respectively. The defect-rich grain boundary is usually the center of electron-hole recombination, which leads to fast quenching of PL intensity herein. Thus, both 2D mapping plots show the grain distribution due to the small difference in the PL intensities. More importantly, the ZnTPY-seeded perovskite film (Fig. 5c) possessed higher PL intensity than the pristine film (Fig. 5d) in an area of 40 μm by 40 μm , suggesting that the enhancement of perovskite crystallinity by ZnTPY CONASHs is homogeneous in a large film area.

Conclusion

We proposed a new perovskite crystallization pathway using a ZnTPY-CONASH additive as a nucleation seed to improve the crystallization and performance of PSC devices. The ZnTPY-CONASH additive was synthesized at a liquid/liquid interface; then, ultrasonic vibration was applied to uncoordinated TPY sites. The additive can chelate PbI_2 for the ZnTPY: PbI_2 complex, which serves as a heterogeneous nucleation seed contributing to a higher conversion efficiency, uniform growth of perovskite crystals, and thus a smoother film surface. Synchrotron GIXS revealed a higher conversion ratio of PbI_2 into the perovskite tetragonal phase with ZnTPY nuclei, and hence the fewer defect sites (residual PbI_2) in the film. Consequently, the defect-less ZnTPY-processed perovskite film exhibited a longer PL lifetime, favoring the PSC performance. Our CONASH additive as a crystallization nucleus provided a novel perovskite crystallization pathway through 2D CONASHs, which might be generalized to the optimization of organic photovoltaic performance.

Author contributions

Y.-C. W., U.-S. J., C.-W. C., K. T., and H. N. conducted and supervised this study. H. M. synthesized the TPY ligand. Y.-C. W., C.-Y. L., and C.-C. W. fabricated PSCs and optimized their performance. C.-J. S., J.-W. C., and U.-S. J. performed the synchrotron-based GIXS measurements. Y.-C. W., C.-H. C., C.-Y. L., C.-C. W., and S.-K. H. conducted data collection, analysis, and explanation. Y.-C. W., C.-H. C., W.-B. J., U.-S. J., C.-W. C., K. T., and H. N. drafted and revised the manuscript. All authors revised the manuscript and agreed to its content.

Conflicts of interest

The authors declare no competing interests.

Acknowledgements

Y.-C. W. is grateful for funding from JSPS-KAKENHI (Grant No. 20K15135) and the ICYS, NIMS for research funding. H. N. acknowledges the financial support from JST-CREST JPMJCR15F2 (Grant No. JP26220801) and JSPS-KAKENHI (Grant No. JP19H05460). C.-W. C. acknowledges the financial support from the Ministry of Science and Technology (MOST), Taiwan (Grant No. 108-2923-M-002-002-MY2, MOST-NIMS add-

on project). This work is also supported by the Center of Atomic Initiative for New Materials (AI-Mat), National Taiwan University, from the Featured Areas Research Center Program within the framework of the Higher Education Sprout Project by the Ministry of Education in Taiwan (108L9008).

References

- 1 M. Kim, *et al.*, Conformal quantum dot- SnO_2 layers as electron transporters for efficient perovskite solar cells, *Science*, 2022, **375**, 302–306.
- 2 J. Wang, *et al.*, Growth of 1D Nanorod Perovskite for Surface Passivation in FAPbI_3 Perovskite Solar Cells, *Small*, 2022, **18**, 2104100.
- 3 Y.-C. Wang, *et al.*, Quantum-assisted photoelectric gain effects in perovskite solar cells, *NPG Asia Mater.*, 2020, **12**, 54.
- 4 A. Y. Alsalloum, *et al.*, Low-temperature crystallization enables 21.9% efficient single-crystal MAPbI_3 inverted perovskite solar cells, *ACS Energy Lett.*, 2020, **5**, 657–662.
- 5 Y.-C. Wang, J. Chang, L. Zhu, X. Li, C. Song and J. Fang, Electron-transport-layer-assisted crystallization of perovskite films for high-efficiency planar heterojunction solar cells, *Adv. Funct. Mater.*, 2018, **28**, 1706317.
- 6 Y. Yang, *et al.*, Modulation of perovskite crystallization processes towards highly efficient and stable perovskite solar cells with MXene quantum dot-modified SnO_2 , *Energy Environ. Sci.*, 2021, **14**, 3447–3454.
- 7 S. S. Li, *et al.*, Intermixing-seeded growth for high-performance planar heterojunction perovskite solar cells assisted by precursor-capped nanoparticles, *Energy Environ. Sci.*, 2016, **9**, 1282–1289.
- 8 C.-Y. Lin, *et al.*, Unveiling the nanoparticle-seeded catalytic nucleation kinetics of perovskite solar cells by time-resolved GIXS, *Adv. Funct. Mater.*, 2019, **29**, 1902582.
- 9 H. Maeda, K. Takada, N. Fukui, S. Nagashima and H. Nishihara, Conductive Coordination Nanosheets: Sailing to Electronics, Energy Storage, and Catalysis, *Coord. Chem. Rev.*, 2022, **470**, 214693.
- 10 S. Xiang, *et al.*, Photocatalytic hydrogen evolution from water based on Zn-terpyridine 2D coordination nanosheets, *J. Mater. Chem. A*, 2022, **10**, 24345–24352.
- 11 S. Liu, *et al.*, Solution-processed organometallic quasi-two-dimensional nanosheets as a hole buffer layer for organic light-emitting devices, *Nanoscale*, 2020, **12**, 6983–6990.
- 12 R. Toyoda, *et al.*, Heterometallic Benzenehexathiolato Coordination Nanosheets: Periodic Structure Improves Crystallinity and Electrical Conductivity, *Adv. Mater.*, 2022, **34**, 2106204.
- 13 Y.-C. Wang, *et al.*, Two-dimensional bis(dithiolene)iron(II) self-powered UV photodetectors with ultrahigh air stability, *Adv. Sci.*, 2021, **8**, 2100564.
- 14 T. Tsukamoto, *et al.*, Coordination nanosheets based on terpyridine-zinc (II) complexes: as photoactive host materials, *J. Am. Chem. Soc.*, 2017, **139**, 5359–5366.
- 15 R. Zhang, *et al.*, Edge-site engineering of defective Fe- N_4 nanozymes with boosted catalase-like performance for retinal vasculopathies, *Adv. Mater.*, 2022, **34**, 2205324.

- 16 M. Huang, *et al.*, MOF-derived bi-metal embedded N-doped carbon polyhedral nanocages with enhanced lithium storage, *J. Mater. Chem. A*, 2017, **5**, 266–274.
- 17 F. Liu, *et al.*, Coordination engineering of metal single atom on carbon for enhanced and robust potassium storage, *Matter*, 2021, **4**, 4006–4021.
- 18 D. B. Mitzi, Templating and structural engineering in organic–inorganic perovskites, *J. Chem. Soc., Dalton Trans.*, 2001, 1–12.
- 19 Z. Cheng and J. Lin, Layered organic-inorganic hybrid perovskites: structure, optical properties, film preparation, patterning and templating engineering, *CrystEngComm*, 2010, **12**, 2646.
- 20 J. Burschka, *et al.*, Sequential deposition as a route to high-performance perovskite-sensitized solar cells, *Nature*, 2013, **499**, 316–319.
- 21 P. Zhang, *et al.*, Photogenerated electron transfer process in heterojunctions: in situ irradiation XPS, *Small Methods*, 2020, **4**, 2000214.
- 22 G. Zhang, S. Li, H. Zeng, S. Zheng and M. C. Neary, Diplumbane-catalysed solvent- and additive-free hydroboration of ketones and aldehydes, *RSC Adv.*, 2022, **12**, 19086–19090.
- 23 P.-W. Liang, *et al.*, Additive enhanced crystallization of solution-processed perovskite for highly efficient planar-heterojunction solar cells, *Adv. Mater.*, 2014, **26**, 3748–3754.
- 24 P. J. Albiety, B. P. Cleary, W. Paw and R. Eisenberg, New cationic iridium(III) complexes of diiodobenzene as electrophilic catalysts: using chelation and lability in concert, *J. Am. Chem. Soc.*, 2001, **123**, 12091–12092.
- 25 P. D. Vellis, J. A. Mikroyannidis, C.-N. Lo and C.-S. Hsu, Synthesis of terpyridine ligands and their complexation with Zn^{2+} and Ru^{2+} for optoelectronic applications, *J. Polym. Sci., Part A: Polym. Chem.*, 2008, **46**, 7702–7712.
- 26 J. Li, Z. Guo, L. Xu and W.-Y. Wong, Synthesis of bis-terpyridine-based metallopolymers and the thermoelectric properties of their single walled carbon nanotube composites, *Molecules*, 2021, **26**, 2560.
- 27 Y.-C. Wang, X. Li, L. Zhu, X. Liu, W. Zhang and J. Fang, Efficient and hysteresis-free perovskite solar cells based on a solution processable polar fullerene electron transport layer, *Adv. Energy Mater.*, 2017, **7**, 1701144.
- 28 H.-C. Chia, *et al.*, Critical intermediate structure that directs the crystalline texture and surface morphology of organo-lead trihalide perovskite, *ACS Appl. Mater. Interfaces*, 2017, **9**, 36897.
- 29 Y. Yun, *et al.*, A nontoxic bifunctional (anti)solvent as digestive-ripening agent for high-performance perovskite solar cells, *Adv. Mater.*, 2020, **32**, 1907123.
- 30 Y. C. Kim, *et al.*, Beneficial effects of PbI_2 incorporated in organo-lead halide perovskite solar cells, *Adv. Energy Mater.*, 2016, **6**, 1502104.
- 31 M.-C. Shih, *et al.*, Spatially resolved imaging on photocarrier generations and band alignments at perovskite/ PbI_2 heterointerfaces of perovskite solar cells by light-modulated scanning tunneling microscopy, *Nano Lett.*, 2017, **17**, 1154–1160.
- 32 D. Bi, *et al.*, Polymer-templated nucleation and crystal growth of perovskite films for solar cells with efficiency greater than 21%, *Nat. Energy*, 2016, **1**, 16142.